Research on drag reduction mechanism of pneumatic subsoiler and establishment of resistance mathematical model

Authors: Li, Xia, Wang, Sichao, Meng, Hewei, Qu, Qingjiang, and Jia, Yunwei

Source: Canadian Journal of Soil Science, 102(2) : 531-548

Published By: Canadian Science Publishing

URL: https://doi.org/10.1139/CJSS-2021-0101

NRC Research Press

ARTICLE

Research on drag reduction mechanism of pneumatic subsoiler and establishment of resistance mathematical model

Xia Li, Sichao Wang, Hewei Meng, Qingjiang Qu, and Yunwei Jia

Abstract: According at the characteristics of large subsoiling resistance and small subsoiling range, a pneumatic subsoiling mechanism was designed to disturb the soil with different air pressure. To achieve the purpose of pneumatic subsoiling, first, the aerodynamic model of subsoiling was established, and then the feasibility of the design was verified by experiments. Using the dynamic telemetry data of the sensor, the effects of tillage depth (25, 30, and 35 cm), pressure (4, 6, and 8 MPa), and working speed (2.5, 3.0 and 3.5 km·h^{-1}) on traction resistance were analyzed. The test results showed that under the condition pneumatic subsoiling, the traction resistance was reduced by 7.28%–22.37%, and the soil disturbance coefficient was 55.49%. The effect of pneumatic subsoiling showed that it has met the design requirements. Pneumatic subsoiling not only improved the problem of small stress of traditional subsoiling but also increased the disturbance of gas to soil on the basis of traditional subsoiling, so as to achieve the effect of subsoiling and reducing resistance and consumption.

Key words: tractive resistance, pneumatic subsoiling, conservation tillage, mathematical-analytical model.

Résumé : Les auteurs ont conçu un système de sous-solage pneumatique qui modifie le sol grâce à une pression d'air variable. Ils se sont fiés pour cela aux propriétés d'une forte résistance et d'une faible étendue du sous-sol. Pour travailler le sous-sol de façon pneumatique, ils ont en un premier temps créé un modèle aérodynamique du sous-sol, puis vérifié la faisabilité du concept par l'expérimentation. Ils ont analysé les effets de la profondeur du travail (25, 30 ou 35 cm), de la pression (4, 6 ou 8 MPa) et de la vitesse (2,5, 3,0 ou 3,5 km·h^{-1}) sur la résistance à la traction à partir des données télémétriques dynamiques prises par le capteur. Les résultats indiquent que le sous-solage pneumatique réduit la résistance à la traction de 7,28 à 22,37%, avec un coefficient de perturbation du sol égal à 55,49%. Les contraintes théoriques ont donc été respectées. Le sous-solage pneumatique non seulement atténue le problème du faible stress qu'engendrent les méthodes de sous-solage classiques, mais permet aussi une plus grande perturbation du sol par les gaz, si bien qu'on obtient le sous-solage désiré tout en réduisant la résistance et la consommation d'énergie. [Traduit par la Rédaction]

Mots-clés : résistance à la traction, sous-solage pneumatique, travail de conservation du sol, modèle d'analyse mathématique.

Introduction

Cultivated land degradation is a worldwide problem. With locust plague, extreme weather, population growth, and other factors, food security will continue to deteriorate in the next few decades. Therefore, the development of conservation tillage (Gordon et al. 1998) is the need for future development. Subsoiling. As an important part of conservation tillage, it can improve the yield of food crops. Because soil tillage will produce plough sole, the soil layer is over compacted, that is, the space between soil aggregates is compressed (Alakukku 1999), which affects the transfer of energy and matter, reduces the permeability of water and nitrogen (N), and makes the crop roots unable to extend

Received 1 August 2021. Accepted 15 October 2021.

X. Li, S. Wang, and Y. Jia. Tianjin Key Laboratory of Advanced Mechanical and Electrical Systems Design and Intelligent Control, School of Mechanical Engineering, Tianjin University of Technology, Tianjin 300384, People's Republic of China; National Experimental Teaching Demonstration Center for Mechanical and Electrical Engineering (Tianjin University of Technology), Tianjin 300384, People's Republic of China.

H. Meng and Q. Qu. School of Mechanical and Electrical Engineering, Shihezi University, Shihezi City, Xinjiang 832061, People's Republic of China.

Corresponding author: Yunwei Jia (email: sumomer@163.com).

downward to obtain nutrients (Cassman et al. 2002). Subsoiling can improve soil texture, reduce soil strength, and effectively promote grain growth (Hipps and Hodgson 1987); After subsoiling, it can achieve the function of water storage and moisture conservation, prevent water and soil loss, drought and flood disasters, so as to adapt to crop root growth and nutrient absorption, facilitate grain growth and improve crop yield (Askari et al. 2019).

The commonly used subsoiling methods include biological subsoiling, bionic drag reduction, and vibration drag reduction. the cost of biological subsoiling is low, but the planting time is long, and the crops stop planting, which reduces the crop yield and economic benefits (Ess et al. 1998); After long-term evolution, organisms in nature have developed excellent structures and functions of drag (Sanchez et al. 2005), Ywa et al. (2020) By changing the structure of subsoiling shovel, a bionic shark subsoiling shovel was designed, which could produce good disturbance to the soil surface and reduce soil water loss, so as to promote the growth of plant roots and effectively improve the soil water absorption; vibration drag reduction is an earlier research method of subsoiling drag reduction, and Bandalan et al. (1999) conducted vibration subsoiling in sugarcane field, and field tests with different vibration frequencies and forward speeds. Compared with nonvibration subsoiling, the efficiency was greatly improved; Hilal et al. (2021) studied the vibration, slip, critical depth (CD), and depth stability ratio (DSR) of the driver seat of an agricultural tractor (VDS) during vibrating and nonvibrating wing of subsoiler at a farm in Mosul, Iraq. The results showed that traction speed and penetration angle had little influence on VDS, while the vibrating wing had great influence on VDS. The results also showed that the increase of tractor speed had a negative impact on VDS, slip ratio, CD, and DSR. Precision agriculture is also the focus of current research. Farmers in the coastal plains of the southeastern United States mainly rely on annual subsoiling, deep treatment, and soil compaction to improve their yield. However, farmers usually do not know if, where and how deep subsoiling is needed from every year (Clark 1999; Raper et al. 2005). Khalilian et al. (2014), in the Clemson instrumented subsoiler shank in coastal plain soils of test, calibrated instruments for subsoiler handle according to cone penetrometer readings for three coastal plain soil types. Finally, the precise depth of subsoiling can be measured, or the position and depth of subsoiling can be controlled in real time to generate a depth map of a specific site. In addition, the structure of subsoiler can be changed to optimize the subsoiler; Usaborisut and Prasertkan (2019) put forward an efficient subsoiling method through the comprehensive analysis of subsoiling rotary rake, which improved the operation quality of the machine and reduced the traction of subsoiler and improved subsoiling efficiency.

Subsoiling is a high-cost mechanized operation (Simoes et al. 2011). The traditional subsoiling shovel has a bending angle of 10° to 20° before and after the blade, which requires a lot of traction and energy in the cultivation process. Therefore, the subsoiling machine needs enough traction to achieve subsoiling drag reduction (Askari et al. 2019); Zhang et al. (1999) designed a pneumatic subsoiling method to break the lower layer of the plow by combining subsoiling shovel and airflow disturbance. A high-pressure gas injection device was added to the subsoiling shovel of the subsoiling machine so that the subsoiling shovel could spray high-pressure gas when the subsoiling machine was working, reducing the friction between the subsoiling shovel and soil, so as to realize the disturbance to the soil. In view of the problems of large resistance and high energy consumption in subsoiling operation, the cost of subsoiling drag reduction is twice that of deep tillage and four times that of ordinary tillage, which increases the additional fuel consumption. In this paper, a device combining pneumatic device and subsoiling shovel was developed to achieve the purpose of subsoiling and reduce energy consumption (Figueiredo and La Scala 2011). Due to the lack of research on the pneumatic subsoiling operation, in this paper, the pneumatic subsoiling operation has been studied based on the crack propagation mechanism. The high-pressure gas was used to shear the soil to break it up, and the plow bottom was cut to break up the soil aggregates. To realize the purpose of subsoiling through gas blasting, the mathematical analysis model of traction force prediction of pneumatic subsoiler was established.

Overall Structure and Gas Explosion Model Hypothesis

Structure design of the whole machine

The three-dimensional model structure of the subsoiler (Lin et al. 2019) is shown in Fig. 1. The main structure takes of the tractor as the power source, through the three-point suspension device will be subsoiler and tractor connected, driving the subsoiler to split the soil, and the air compressor of the pneumatic subsoiler was connected with the subsoiler frame, tractor frame, traction suspension, and shovel handle frame. Pneumatic split subsoiler is composed of air compression device and subsoiling depth regulating device.

The pneumatic subsoiling shovel is mainly composed of sliding cutting shovel handle, shovel tip, and connecting adjustment device. The pneumatic subsoiling shovel is located on the rear cross element of the frame. Pneumatic subsoiler uses the principle of air pressure splitting to achieve subsoiling and drag reduction. Set the air compressor time t, exhaust air volume V, and the working state of the air duct is shown in Fig. 2.

Fig. 1. Three-dimensional model of subsoiler. (1) Tractor. (2) Traction suspension. (3) Cylinder. (4) Frame. (5) Subsoiler. (6) Depth regulator. (7) Depth limiting wheel. (8) Wheel.

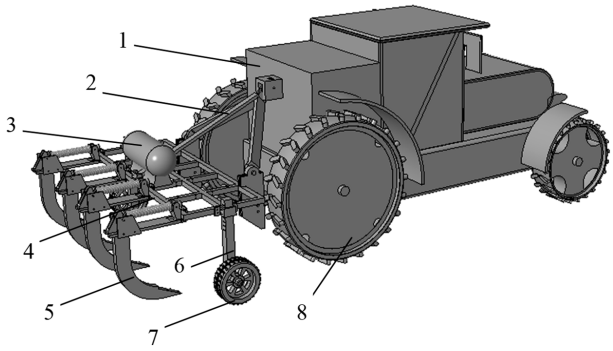

Working principle

The soil is broken under the instantaneous impact of high-pressure gas transported by air compressor, airway, and subsoiler. The soil is damaged and deformed, and the pneumatic subsoiling operation is completed, as shown in Fig. 3. The plastic flow model on the soil surface is as follows:

Crack propagation mechanism

Cracks were generated by high-pressure pneumatic force in the soil, and the gas viscosity was low so that the pneumatic splitting of soil had higher permeability and pressurization rate (Alfaro and Wong 2001). To assume that the soil is a homogeneous isotropic linear elastomer, the pneumatic subsoiling process is regarded as a static process, and the splitting of the pneumatic subsoiling soil is regarded as a circular hole expansion problem. The stress of the simplified soil is shown in Fig. 4. The pressure P_t in the circular hole expands outward; when P_t increases, the soil around the circular hole evolves from elastic state to plastic state. With the increases of P_t, the area of plastic state expands at the same time. And the radial stress of soil element σ_r increases and the tangential stress σ_θ decreases.

Assume that cracks are caused by compressed soil (Puppala 1998). There are two failure forms in the round hole expansion problem, one is tensile failure, which is manifested in the lifting of the original soil surface, as shown in Fig. 5*a*, and the other is shear failure, which is manifested in the soil disturbance caused by extrusion in the deep soil layer inside the soil (Murdoch 2002), as shown in Fig. 5*b*. In practical operation, the above two points will occur simultaneously. The dominant mode is tension failure or shear failure.

Tension failure mechanism

When tensile failure occurs, the negative value of effective small stress is numerically larger than the tensile strength of soil, and it is assumed that the soil is an elastomer. There is a criterion for judging the tension failure of soil. There is the following formula for tensile failure of soil (Jawoski et al. 1981):

$$(1) \qquad \sigma_3' \leq -\sigma_t$$

where σ_3' is the effective minimum principal stress of soil mass, MPa; σ_t is the tensile strength of soil mass, MPa.

According to the mechanical relationship of circular hole expansion, the maximum radial stress of soil element $\sigma_{r\max}$ and minimum tangential stress $\sigma_{\theta\min}$ is:

$$(2) \qquad \sigma_{r\max} = P_t$$

$$(3) \qquad \sigma_{\theta\min} = 3\sigma_3 - \sigma_1 - P_t$$

If the soil has been assumed to be a linear elastomer, there are:

$$(4) \qquad \Delta\sigma_r = -\Delta\sigma_\theta$$

$$(5) \qquad \Delta\sigma_r = \Delta\sigma_1$$

$$(6) \qquad \Delta\sigma_\theta = \Delta\sigma_3$$

where σ_1 is the maximum principal stress perpendicular to the plane of circular hole, MPa; σ_3 is the minimum principal stress perpendicular to the plane of circular hole, MPa.

The criterion of soil tension failure is:

$$(7) \qquad 3\sigma_3 - \sigma_1 - P_t \leq -\sigma_t$$

Because the soil is isotropic, there is $\sigma_1 = \sigma_3$. The pressure P_t in the round hole is:

$$(8) \qquad P_t \geq 2\sigma_3 + \sigma_t$$

The splitting force P_f caused by tensile failure of soil mass is:

$$(9) \qquad P_f = 2\sigma_3 + \sigma_t$$

Soil shear failure mechanism

According to Mohr–Coulomb's soil strength theory, the compressive stress appears due to the pressure of tools on the soil. Where the stress exceeds the cohesion related to soil strength, the crack in the soil wedge breaks under the action of shear angle, and the unit contact stress is σ_1 and σ_3. Using σ-τ, the coordinate representation of the molar stress circle in the coordinate system is shown in Fig. 6.

In the equilibrium state, the soil shear strength envelope τ_f is tangent to the molar stress circle. Point A represents that the shear force is equal to the shear strength. The molar stress circle at point A is the limit stress circle. According to Mohr–Coulomb soil strength

Fig. 2. Pneumatic schematic diagram of airway.

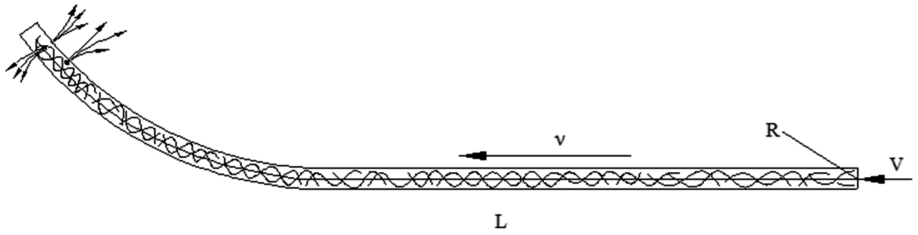

Fig. 3. Surface plastic flow model.

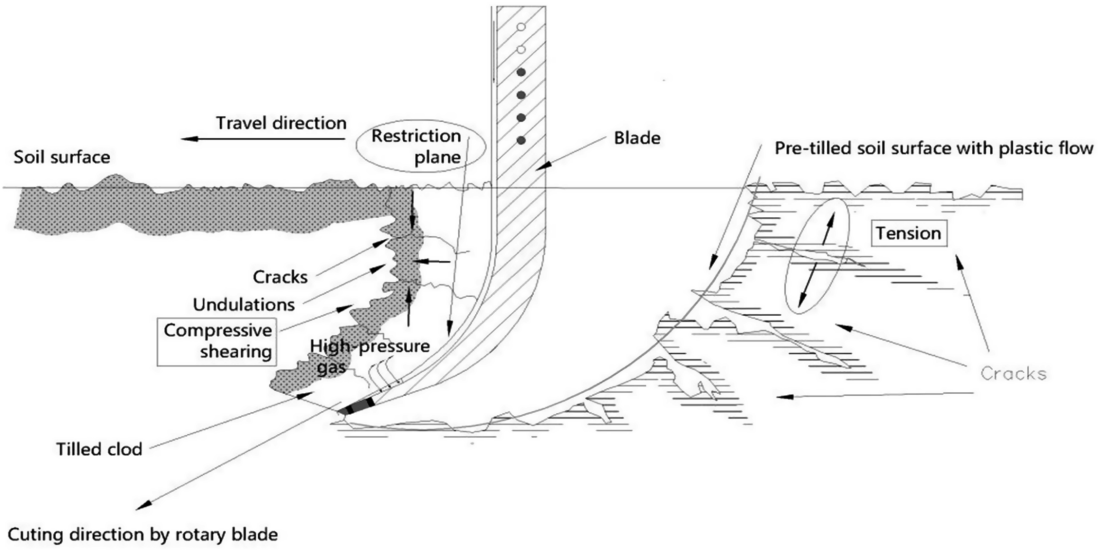

Fig. 4. Schematic diagram of pressure expansion in soil circular hole.

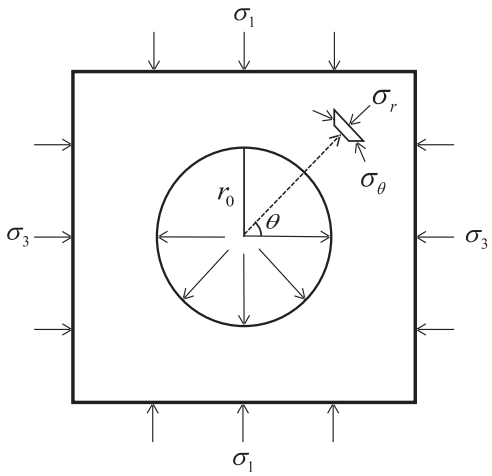

theory, the soil shear strength envelope τ_f equation is as follows:

$$\tau_f = \sigma \tan\varphi + c \quad (10)$$

where σ is the normal stress on tangent sliding surface, MPa; φ is soil friction angle, °; C is the soil cohesion, MPa.

Geometric relationship of molar stress circle:

$$\begin{aligned} AO_1 &= \frac{1}{2}(\sigma_1 - \sigma_3) = BO_1 \cdot \sin\varphi \\ &= (BO + OO_1)\cdot\sin\varphi = \left[c\cdot\cot\varphi + \frac{1}{2}(\sigma_1 + \sigma_3)\right]\cdot\sin\varphi \end{aligned} \quad (11)$$

Sorting results:

$$\sigma_1 - \sigma_3 = (\sigma_1 + \sigma_3)\sin\varphi + 2c\cdot\cos\varphi \quad (12)$$

The stress state of soil mass conforms to eqs. 2 and 3, so there is:

$$P_t = \frac{1}{2}(3\sigma_3 - \sigma_1)(1 + \sin\varphi) + c\cdot\cos\varphi \quad (13)$$

Considering the soil as an isotropic body, there is $\sigma_1 = \sigma_3$. The splitting force P_f causing shear failure of soil mass is:

$$P_f = \sigma_3(1 + \sin\varphi) + c\cdot\cos\varphi \quad (14)$$

Fig. 5. Failure form and mechanism diagram. (*a*) Mechanism diagram of crack lifting. (*b*) Fracture shear mechanism diagram. [Colour online.]

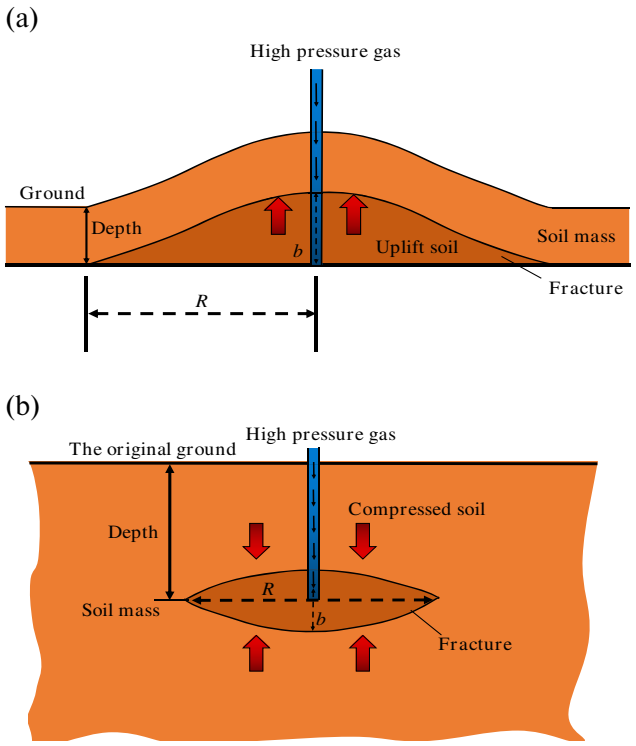

Fig. 6. Molar stress circle.

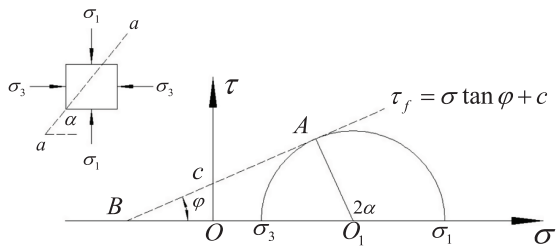

According to eqs. 9 and 14, in pneumatic subsoiling, cracks appear in the soil under the action of pressure in the round hole, and the internal pressure increases, the radial stress of soil element σ_r increases, as well as tangential stress σ_θ. The principal stress of the soil element is directly proportional to the depth of the soil. When the gas explosion is deep, the principal stress of the soil element at this depth is large. At this time, the soil splitting is mostly caused by shear failure. The soil after gas explosion compresses up and down along the center of the circular hole, extends, and expands in the horizontal direction to form cracks. The slow deceleration rate of air pressure decline leads to the large expansion radius of cracks, which is conducive to soil subsoiling improve the subsoiling effect.

Fig. 7. Fracture propagation model of air pressure subsoiling.

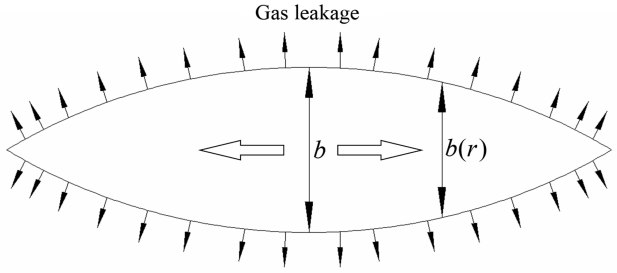

Gas explosion model assumptions

First, it can be considered that the cracks are mainly uplifted soil, and the compression deformation can be ignored; When the modulus of soil is small, the cracks are mainly caused by soil compression, and the deformation caused by uplift can be ignored; The expansion range of soil cracks at the splitting point is horizontal (Murdoch 2002), which is approximately circular. When the crack propagates to a certain range, the development direction of the crack is related to the stress state of the soil at the site. Assuming that the crack propagation model is correct, the results showed that at the tuyere, the air gap began to expand horizontally along the radial direction, which was approximately circular. The soil was homogeneous, isotropic, and elastic, and the direction of gas leakage was vertical. Gas leakage law conforms to Darcy's law. Heat conduction during crack propagation is not considered (Murdoch 2002). The simplified diagram of pneumatic subsoiling fault propagation model is shown in Fig. 7.

The crack propagation radius is described according to the soil displacement model equation. According to the statistical results of Murdoch, the following relationship (Murdoch 2002):

$$\sqrt{\frac{b(r)}{b}} + \left(\frac{r}{R}\right)^2 = 1 \quad (15)$$

where $b(r)$ is the crack width at r from gas explosion center, mm; b is the crack displacement, mm; R is the crack diameter and width, mm.

$$b = \frac{3PR^4}{8H^3E} \quad (16)$$

where P is the gas explosion pressure, MPa; H is the gas explosion depth, m; E is the soil firmness, MPa.

The equation of crack width $b(r)$ at the distance r from the gas explosion center is obtained by simultaneous eqs. 15 and 16:

$$(17)\quad b(r)=\frac{3PR^4}{8H^3E}\left[1-\left(\frac{r}{R}\right)^2\right]^2$$

Pneumatic subsoiling evaluation method

After subsoiling, the soil profile perpendicular to the forward direction of the subsoiler was cut to measure the surface line of the cultivated land, the surface line of the cultivated land, and the bottom line of the actual subsoiling ditch, and the soil fluffy degree p and soil disturbance coefficient γ were calculated. It can be calculated respectively according to the following formula (Hang et al. 2017):

$$(18)\quad p=\frac{A_h-A_q}{A_q}\times 100\%$$

$$(19)\quad \gamma=\frac{A_s}{A_q}\times 100\%$$

where p is the soil swelling, %; A_q, Ah are the cross-sectional area from the surface before and after tillage to the theoretical subsoiling ditch bottom, mm^2; γ is the soil disturbance coefficient, %; A_s is the cross-sectional area from the surface before tillage to the actual subsoiling ditch bottom, mm^2.

Stress analysis of gas explosion subsoiling

According to the fitting between the traditional subsoiling shovel and the soil stress model, the relevant equations were established. Considering the lifting tension and shear failure force of the soil, the relevant mechanical models were established, as shown in Fig. 8, and the equilibrium equations were listed. Under the action of pneumatic subsoiling, the crack direction of the soil is the same as that of the subsoiler. According to Ahmadi (2017), the traction force (F_d) of the subsoiler can be divided into three parts: soil cutting force (F_c), friction force (F_f) between the subsoiler, and the soil and inertia force (F_i) generated by the displacement of soil failure wedge. However, this study uses pneumatic subsoiling to blast the plow bottom of the soil. High pressure air force (F_g) was introduced, so the traction force of subsoiler was divided into four parts. When the subsoiler is working, it will disturb the soil along with the movement of the tractor, forming a soil wedge (as shown in Fig. 8).

Air pressure intensity model

Based on the mathematical analysis of the traditional subsoiling by Jiang et al. (2020), the pneumatic subsoiling mathematical model was obtained. The soil was differentiated into elements. The element cutting force (dF_c), element soil weight (dW), element soil shear strength (dR), and element soil air pressure strength (dF_g) are distributed on each element (Fig. 9). Both the lifting force and shear force are greater than the shear strength of the failure surface before the soil. Under the self-weight of soil mass and cutting force, the soil wedge is destroyed, which meets the following equation:

$$(20)\quad \overrightarrow{dF_c}+\overrightarrow{dR}+\overrightarrow{dW}+\overrightarrow{dF_g}=0$$

As high-pressure air flow presents a horizontal diffusion state in the soil transmission process, and the crack penetration presents an elliptical shape, as shown in Fig. 7, the soil is assumed to be an elastomer, S_1 is the horizontal diffusion area, and the effective area acting on the lifting of cotton shoveling soil is expressed as:

Fig. 8. Subsoil wedge model. L_1 in the figure is the first length of soil wedge surface; L_2, second length of soil wedge; R, radius of subsoil wedge; θ, center angle of subsoil wedge; ε, angle between failure plane and horizontal plane; h, is the working height from the subsoiling shovel to the top of the soil wedge. [Colour online.]

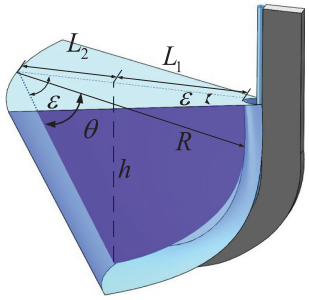

Fig. 9. Three-dimensional failure model of soil. The subsoiling shovel angle is ω, that is, the angle of the gas pressure perpendicular to the horizontal plane; β is the angle between F_c and the horizontal plane; ε is the angle between the failure plane and the horizontal plane. [Colour online.]

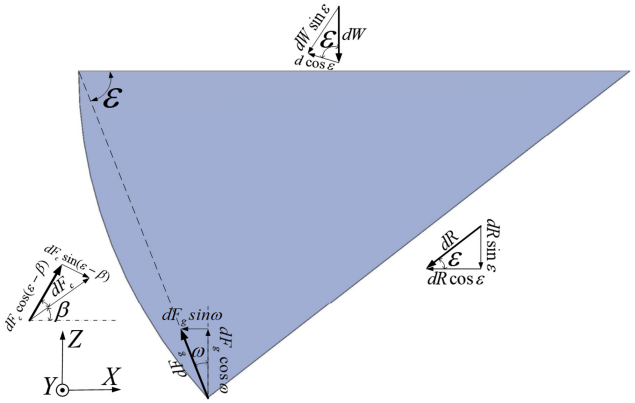

Fig. 10. Displacement of *O*-point caused by expansion of circular cavity in half plane. σ_p is the stress at the outer boundary of the plastic zone; R_c is gas jet radius; R_p is the radius of the plastic zone; h is the distance from the ground to the center of horizontal jet pressure. [Colour online.]

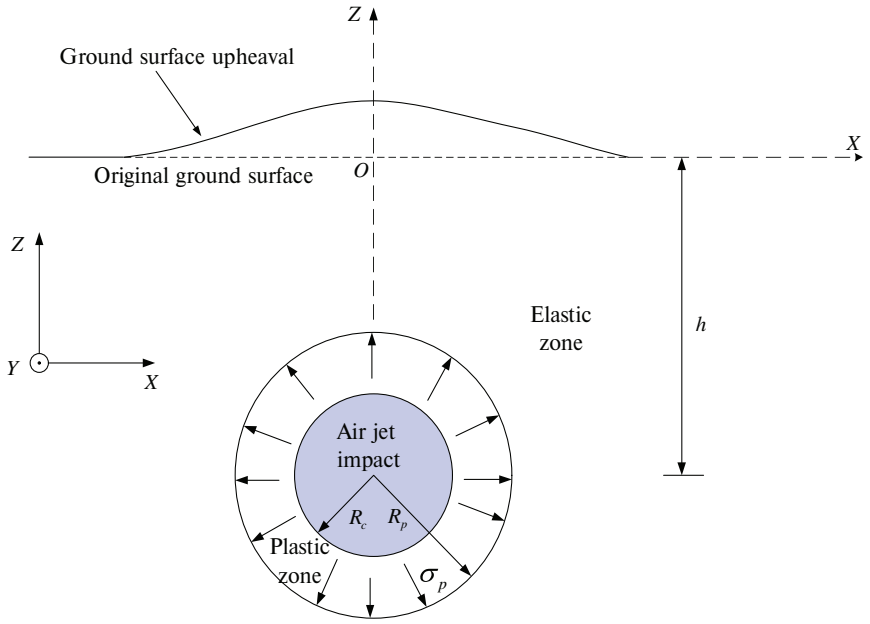

$$S_1 = \pi\left(\frac{b(r)}{2}\right)^2 \quad (21)$$

According to the high-pressure gas distribution equation proposed by Nautiyal (1994), the distribution at its gas injection point is:

$$P_{n+1} = \left[P_n^2 - 12P_nQ\mu_{gas}\ln\left(\frac{r_{n+1}}{r_n}\right)\Big/(\pi g\rho h^3)\right]^{\frac{1}{2}} \quad (22)$$

where P_{n+1} is the high-pressure gas pressure at the gas injection point r_{n+1} (MPa); P_n is the high-pressure gas pressure at r_n the gas injection point (MPa); high pressure gas pressure at the gas injection point is r_n of Q (MPa), Q is the flow between gas injection point r_{n+1} and gas injection point r_n ($m^3 \cdot s^{-1}$); μ_{gas} is the viscosity coefficient of high pressure gas; ρ is the gas density ($kg \cdot m^{-3}$).

Substitute eq. 21 into eq. 17 to obtain the air pressure at P_{n+1}. Assuming that the pressure difference of gas in the ideal state presents a circular distribution according to the distance from the gas injection point, the effective area of soil lifting caused by gas acting on the fracture surface is countless n small rings, and the distribution pressure of soil crack expansion and lifting can be expressed as:

$$F_g = PS_1 = \sum_{r=r_0}^{r_n=R} P_n\left[\pi(r_{n+1}^2 - r_n^2)\right] \quad (23)$$

The calculation formula of F_g in the working direction is as follows:

$$F_{g,x} = F_g \cdot \sin\omega \quad (24)$$

Soil wedge displacement model

Because the upward lifting force F_i decreases under the action of pneumatic subsoiling, in the actual test process, the soil lifting will exceed the height of nonpneumatic subsoiling, and the soil lifting height will increase under the action of pneumatic force, as shown in Fig. 10.

According to the analysis of soil uplift by Wang et al. (2019), upward is the deformation coefficient at the boundary of the soil plastic zone, r_A is the distance from the horizontal jet pressure center to point *O* in the elastic zone, $r_A = (z^2 + (h+x)^2)^{0.5}$; u_{zO} is the upward lifting distance of the soil during the aerodynamic process, u_{xO} is the lateral displacement distance of the soil during the aerodynamic process, Z represents the distance from the gas explosion point to the Z-axis of point *O*, and X represents the distance from the gas explosion point to the X-axis of point *O*. The formula is as follows:

$$u_{zO} \approx u_p \frac{b(r) + u_p}{2r_A + u_p(b(r)/2r_A)} \cdot \frac{z}{r_A} \quad (25)$$

$$u_{xO} \approx u_p \frac{b(r) + u_p}{2r_A + u_p(b(r)/2r_A)} \cdot \frac{h+x}{r_A} \quad (26)$$

i_z is the soil lifting movement, dh is the soil lifting displacement during subsoiling, and its displacement formula is:

$$(27) \quad i_z = u_{z0} + \int dh$$

i_x is the lateral movement of soil, dv is the lateral displacement of soil during subsoiling, and the displacement formula is:

$$(28) \quad i_x = u_{x0} + \int dv$$

In the process of pneumatic subsoiling, the soil wedge will move in a certain direction under the action of air pressure (as shown in Fig. 10). However, because the soil is an uneven porous medium, the high-pressure air flow penetrates into the soil along the crack and expands in a certain direction. At the same time, the discontinuity of the soil makes the diffused air flow easy to leak from the soil surface, resulting in air pressure attenuation and the crack width decreases gradually. Therefore, air blasting can be regarded as the coupling of three processes: soil deformation, air pressure attenuation, and gas leakage. Assuming that the subsoiling machine produces an object with the same volume of soil wedge during subsoiling, it is calculated by the principle of impulse and momentum (Ferdinand et al. 2007). The displacement of soil wedge during pneumatic subsoiling is shown in Fig. 11. The total force (F_i) caused by soil wedge displacement is as follows:

$$(29) \quad F_i = \frac{dm}{dt}u - dF_g \cdot \cos\omega \cdot \sin\varepsilon$$

where ε is the angle of the failure plane, di_z is the rising speed of the soil wedge, and di_x is the lateral moving speed of the soil wedge, ε. The value is calculated as:

$$(30) \quad \arctan\frac{\frac{di_z}{dt}}{\frac{di_x}{dt}} = \varepsilon$$

where $\frac{dm}{dt}$ is the discharge speed of the soil inside the soil wedge, u is the cutting speed of the soil relative to the lower surface of the control volume, and the value of u is calculated as:

$$(31) \quad u = \frac{di_z}{\sin\varepsilon dt} = \frac{di_x}{\cos\varepsilon}$$

$$(32) \quad \frac{dm}{dt} = \rho g\frac{dV}{dt} = \rho g A s\frac{di_z}{dt}$$

The calculation formula of F_i in the working direction is as follows:

$$(33) \quad F_{i,x} = F_i\cos\varepsilon$$

Fig. 11. Displacement of soil wedge relative to control volume. [Colour online.]

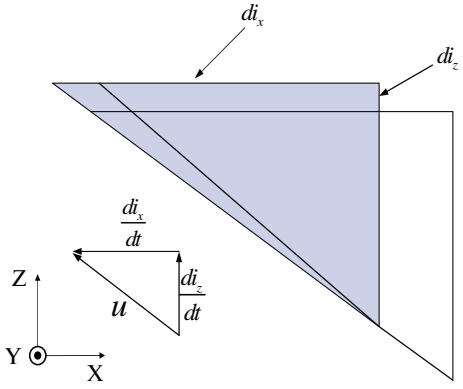

Fig. 12. Soil resistance on subsoiling shovel. b, is the width of subsoiling shovel handle; t, is the thickness at which the shovel handle is loosened. [Colour online.]

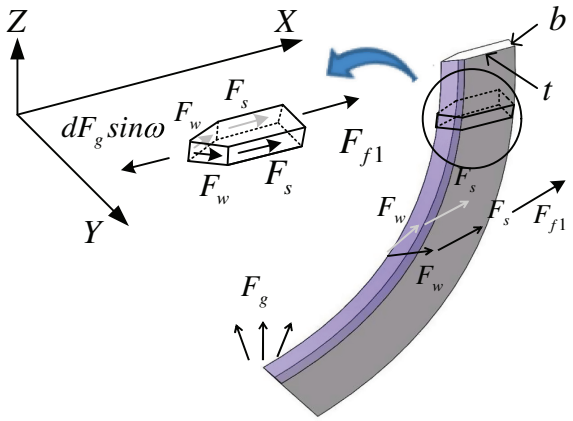

Soil cutting force strength model

Based on the analysis of the element level by Jiang et al. (2020), the following relationship can be obtained:

$$(34) \quad dF_c \cdot \cos(\varepsilon - \beta) = dW \cdot \sin\varepsilon + dR + dF_g \cdot \sin\varphi \cdot \cos\varepsilon$$

$$(35) \quad dW = \rho g dV$$

In the above formula, ρ is the density, g is the acceleration, dV is the soil element volume, and the equation of dV is:

$$(36) \quad dV = \frac{S_2 b}{2\sin\varepsilon}d\delta + \frac{1}{3}S(L_1 + L_2)d\delta$$

L_1 and L_2 are the first and second lengths of the soil wedge surface, and S_2 is the rotating surface area:

$$(37) \quad S_2 = \frac{2L_1 + L_2}{2}(h + u_{z0}) - \left[\frac{(h + u_{z0})L_1}{2} - \left(\frac{\theta R^2}{2} - \frac{R^2\sin\theta}{2}\right)\right]$$

$$L_1 = 2(R + u_{x0}) \cdot \sin^2 \frac{\theta}{2} \tag{38}$$

$$L_2 = (h + u_{z0}) \cdot \cot \varepsilon \tag{39}$$

According to the shear force analysis of Ahmadi (2017), combined with eq. 14, the following relationship is obtained:

$$dR = CA_h + (dF_c \sin(\varepsilon - \beta) + dW \cos \varepsilon) \tan \varepsilon - (\sigma_3(1 + \sin \varphi) + c \cdot \cos \varphi) \cdot A_s \tag{40}$$

where A_h is the cross-sectional area of disturbed soil, and the formula is as follows (Jiang et al. 2020):

$$A_h = \frac{2\left(L_1 + L_2 + \dfrac{b}{2 \sin \varepsilon}\right) \sin \varepsilon + S_2}{2} \tag{41}$$

In combination with eqs. 14, 34, 35 and 41, there are the following formulas:

$$dF_c = \frac{CA_h + \rho g dV(\sin(\varepsilon - \beta) + \cos \varepsilon \cdot \tan \varepsilon) - (\sigma_3(1 + \sin \varphi) + c \cdot \cos \varphi) \cdot A_s}{(\cos(\varepsilon - \beta) - \sin \varepsilon) \cdot \tan \varepsilon} \tag{42}$$

where A_s is the scanning area of soil, and the formula is as follows:

$$A_s = \varepsilon(L_1 + L_2)\left(L_1 + L_2 + \frac{b}{\sin \varepsilon}\right) \tag{43}$$

R and θ are the radius and center angle of the soil wedge formed by the subsoiler, the component (F_c, x) in the working direction of F_c is calculated by dF_c:

$$F_{c,x} = \int_0^{2\varepsilon} \cos \beta \cos \varepsilon \cdot dF_c \tag{44}$$

Soil friction strength model

The friction on the subsoiler comes from handle friction (F_{f1}) and sweeping friction (F_{f2}) (Jiang et al. 2020). F_{f1} consists of two parts: soil metal friction (F_s) and soil internal friction (F_w). However, due to the disturbance of pneumatic subsoiling, F_s decreases or disappears, and there will be a semipermanent soil wedge on the front surface of subsoiling shovel. The application of friction force is shown in Fig. 12, which can be calculated by the formula:

$$F_{f1} = 2(F_s + F_w \cos \varepsilon) - dF_g \cdot \sin \varphi \tag{45}$$

The formula for calculating F_w and F_s according to the soil internal component of handle friction (Ahmadi, 2017) is as follows:

$$F_s = \int_0^{\theta} dFs = \tan \mu \cdot \sigma_h \frac{2Rt + t^2}{2} \theta \tag{46}$$

$$F_w = \int_0^{\theta} dF_w d\theta = (\cos \varepsilon)^{-1} \tan \varphi \cdot \sigma_h \left(\frac{Rb}{2 \tan \varepsilon} - \frac{b^2}{8 \tan^2 \varepsilon}\right) \theta \tag{47}$$

According to Ahmadi's (2017) analysis on the side orientation of the shovel handle: where μ is the soil metal friction angle, φ is the soil friction angle, σ_h is the horizontal normal stress when the shovel occurs, with the following formula (Coduto 2001):

$$\sigma_h = K_p \sigma_v + 2C\sqrt{K_p} \tag{48}$$

σ_v is the vertical normal pressure of soil, and the horizontal normal stress of damaged soil will be calculated according to eqs. 36 and 37, and the formula of K_p is:

$$K_p = \frac{(\cos \varepsilon)^2}{\cos \delta \left[1 - \sqrt{\dfrac{\sin(\delta + \varphi) \sin \varphi}{\cos \delta}}\right]^2} \tag{49}$$

K_p is a dimensionless coefficient, which reflects the relationship between horizontal normal stress and vertical normal stress. Since tension failure and shear failure will occur in the process of pneumatic subsoiling, gas–solid coupling will occur. However, this paper assumed that the soil was elastic, so the soil was isotropic $\sigma_v = \sigma_3$. There are the following formulas:

$$\sigma_h = K_p \frac{p_t - C \cdot \cos \varphi}{1 + \sin \varphi} + 2C\sqrt{K_p} \tag{50}$$

Since the effect of pneumatic subsoiling on soil can be shown as tension failure and shear failure, the analysis of F_{f2} in eqs. 9 and 33 can be calculated by the following formula:

$$F_{f2} = (N_s - P_f) \tan \mu = -(\rho g R \sin \theta + dR) \cdot A_s \cdot \tan \mu \tag{51}$$

N_s is the normal phase force, A_s is the scanning area, and the formula of total friction is as follows:

$$F_f = F_{f1} + F_{f2} \tag{52}$$

The traction force obtained by integrating the above formulas is:

$$F_d = F_{c,x} + F_f + F_{i,x} - F_{g,x} \tag{53}$$

Fig. 13. Pneumatic subsoiler. [Colour online.]

Test Analysis

Test site

On 25 October 2017, the field experiment was carried out in the Wulian experimental field of the teaching experimental field of Shihezi University. The former crop of the experimental field was cotton. During the experiment, the drip irrigation belt was recovered, but the residual film was not recovered, and the soil hardness was too high. The experimental materials include pneumatic subsoiler prototype, Shanghai New Holland SNH1004 tractor, field mechanical telemeter, Field Scout SC900 soil depth hardness meter of American spectrum company, several benchmarks, leather tape, tape, stopwatch, and several sealing bags. The pneumatic subsoiler used in the field test is shown in Fig. 13, and the measured model parameters are shown in Table 1.

During the field experiment, relatively flat and no-tillage land was selected, and the experimental area was planned according to the pre-planned experimental design scheme. A length of 60 m was selected in the experimental field. The flat land with a width of 50 m was used as the test area, and a 10 m long adjustment area was reserved on both sides of the length and width direction of the tractor working state adjustment area, so as to ensure that the tractor works in the predetermined area. At the same time, to eliminate the randomness of point taking, the equidistant point taking method was used to measure points. Fig. 14 below shows the layout of the test area and measuring points.

Test scheme

There are many factors affecting tillage resistance of pneumatic subsoiler, such as tillage depth, shape of subsoiler, forward speed of subsoiler, air pressure, and soil conditions. Aday and Ramadhan (2019) tested three subsoilers and four working depths (30, 40, 50, and 60 cm), and finally obtained different tractions at different depths. In this paper, three factors of different tillage depth, air pressure, and working speed were selected to carry out a full combination test on the tillage resistance of pneumatic subsoiler. The factor level table of the full combination test is shown in Table 2. At the same time, no tillage was used as the test control group.

The tests are grouped according to Table 2. According to eq. 52, the higher the air pressure, the stronger the soil blasting capacity, which has a significant impact on soil fragmentation and the reducing of the subsoiling shovel resistance. The design of the test scheme is shown in Table 3.

Data acquisition

During the test, the field mechanical telemetry was installed on the pneumatic subsoiler and tractor, and the tractor was used as the power source of the pneumatic subsoiler (Jia et al. 2016). The field mechanical telemetry was installed between the pneumatic subsoiler and the tractor. The force measuring device of the telemeter was mainly composed of an upper pull rod with a sensor and a lower suspension pin with sensor. The measurement range of each sensor was 30 kN and the sensitivity was 0.1%. The installation of telemetry sensor is shown in Fig. 15.

Results and Discussion

Change of traction resistance of pneumatic deep Panasonic

Plot the tillage resistance data of pneumatic subsoiler measured by telemetry, as shown in Fig. 16. Test group F_1 to F_9 was measured and relevant data were obtained according to the air pressure group. Taking F_1 as the sample, it can be seen from the figure that no matter what air pressure method is adopted, the traction resistance of pneumatic subsoiling is significantly less than that of nonpneumatic subsoiling, indicating that the pneumatic subsoiling has obvious drag reduction effect. However, under different tillage depth and tillage speed, different air pressure has different effects on reducing traction resistance.

The results showed that under the same tillage depth, soil resistance increased with the increase of tillage depth. With the increase of air pressure, the drag reduction rate of subsoiling increased (Fig. 17). There were

Table 1. Soil and model parameters.

Parameter	Definition	Value
Subsoiler parameters		
	Shape and size (length × width × height)·cm^{-1}	285.1 × 120.7 × 119.14
	Machine weight·kg^{-1}	5800
	Number of subsoiler handles	2
	Adjustable subsoiling shovel range·cm^{-1}	14∼22
	Adjustable range of subsoiling air pressure·MPa^{-1}	0∼8
	Supporting power·kw^{-1}	2.2
State parameters		
P (MPa)	Working pressure	4.0, 6.0, 8.0
V (Km·h^{-1})	Forward speed	2.5, 3.0, 3.5
h^* (cm)	Working depth	30, 35, 40
ρ (kg·m^{-3})	Soil bulk density	1600
C (MPa)	Soil cohesion	28 200
α (rad)	Internal friction angle of soil	0.492
μ (rad)	Soil metal friction angle	0.349
ω (rad)	Included angle between subsoiling shovel and horizontal plane	0.262
β (rad)	Angle between cutting force and horizontal plane	0.524
w (cm)	Width of subsoiler handle	6
t (cm)	Thickness of subsoiler handle	13
A_s (cm)	Sweep width	15
R, θ, u_p		
R (cm)	Radius of soil wedge formed by subsoiler	$30 < R < 60$
θ (rad)	Center angle of soil wedge formed by subsoiler	$0.90 < \theta < 2.00$
u_p[†]	Deformation coefficient at the boundary of soil plastic zone	$u_p \geq 17$

*$h = R\sin\theta$.
[†]u_p is dimensionless.

Fig. 14. Layout of test area and test points. Δ — Measuring points of soil bulk density and soil firmness. □ — Traction force measuring point.

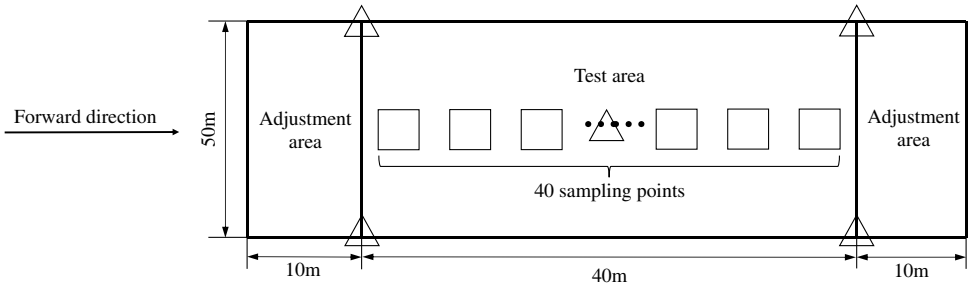

Table 2. Test factor table.

Factor	Level		
Deep tillage (cm)	30	35	40
Speed (km·h^{-1})	2.5	3	3.5
Air pressure (MPa)	4	6	8

different drag reduction effects under different pneumatic subsoiling conditions. The analysis is shown in Table 4.

According to the appeal data, when the tillage depth is the same, the resistance increases with the increase of tillage speed. At the same tillage depth and speed, the traction resistance tends to decrease with the increase of air pressure. The main reason is that the instantaneous blasting force of high-pressure gas breaks the adjacent soil layer and reduces the subsoiling resistance, which reflects that the increase of air pressure has a positive effect on the reduction of traction resistance.

Table 3. Test plan table.

Test number	Deep tillage (cm)	Speed ($km \cdot h^{-1}$)	Test number	Deep tillage (cm)	Speed ($km \cdot h^{-1}$)	Test number	Deep tillage (cm)	Speed ($km \cdot h^{-1}$)	Pressure type
F_1		2.5	F_4		2.5	F_7		2.5	No pressure Pressure I Pressure II Pressure III
F_2	30	3.0	F_5	35	3.0	F_8	40	3.0	No pressure Pressure I Pressure II Pressure III
F_3		3.5	F_6		3.5	F_9		3.5	No pressure Pressure I Pressure II Pressure III

Fig. 15. Traction force measuring device. (*a*) Lower suspension sensor. (*b*) Upper link sensor. [Colour online.]

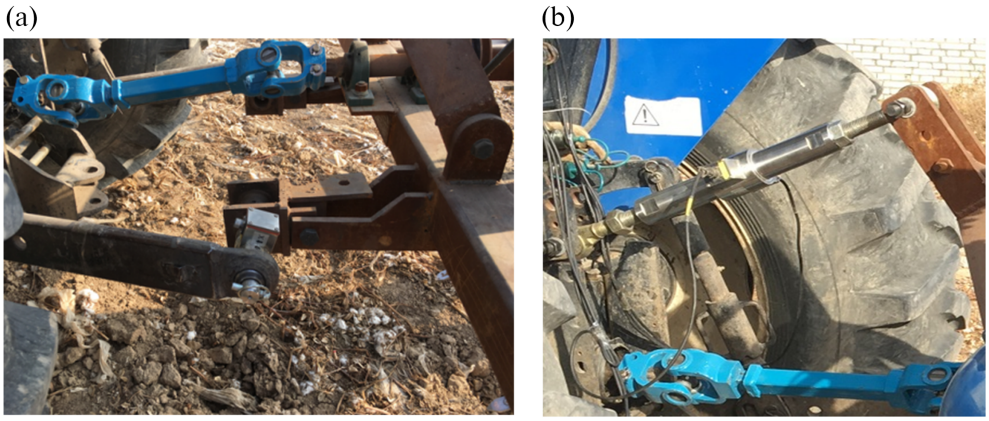

The main reason for the reduction of traction resistance is that the instantaneous blasting force of high-pressure gas destroys the plow bottom and reduces the subsoiling resistance, indicating that the increase of air pressure plays a positive role in reducing traction resistance. Pneumatic subsoiling can effectively reduce the traction resistance regardless of working speed and working depth (as shown in Fig. 18). The average value of different traction resistance caused by different air pressure is shown in Table 5.

Comparison between model verification and the field experimental results

The simulation test of pneumatic under different air pressure, depth, and working speed was carried out to explore the relationship between actual traction force and simulated traction force. Excluding the effect of pneumatic subsoiler, the traction force increases with the increase of depth and speed. But in pneumatic deep panasonic, the greater the air pressure, the smaller the traction. The comparison between simulated pneumatic subsoiling traction resistance rate (SPR) and actual pneumatic subsoiling traction resistance rate (PR) is shown in Fig. 19, the predicted pneumatic subsoiling traction resistance was higher than the actual pneumatic subsoiling traction resistance.

In the process of pneumatic subsoiling, when the air pressure changes differently, the variation range also changes greatly. The working depth increased from 30 cm to 35 cm and then to 40 cm, the working speed increased from 2.5 to 3 $km \cdot h^{-1}$ and then to 3.5 $km \cdot h^{-1}$, the actual traction resistance decreased by 7.28% when the actual working air pressure was 4 MPa, and 13.78% when the actual working air pressure was 6 MPa. When the actual working pressure was 8 MPa, the actual traction resistance decreased by 22.37%. The predicted traction resistance was generally greater than the actual traction resistance. When the predicted working pressure was 4 MPa, the predicted traction resistance decreased by 9.79%, when the predicted working pressure was 6 MPa, the predicted traction resistance decreased by 14.49%, and when the predicted working pressure was 8 MPa, the predicted traction resistance decreased by 31.79%. The field test showed that the drag

Fig. 16. Subsoiling resistance line diagram. The error bar represents the measurement standard deviation of each sampling pneumatic subsoiling traction resistance. This legend is the sample data of F_1. (*a*) Measured at a depth of 30 cm, an air pressure of 0 MPa and a working speed of 2.5 km·h^{-1}. (*b*) Measured at a depth of 30 cm, a pressure of 4 MPa and a working speed of 2.5 km·h^{-1}. (*c*) Measured at a depth of 30 cm, a pressure of 6 MPa and a working speed of 2.5 km·h^{-1}. (*d*) Measured at a depth of 30 cm, an air pressure of 8 MPa and a working speed of 2.5 km·h^{-1}.

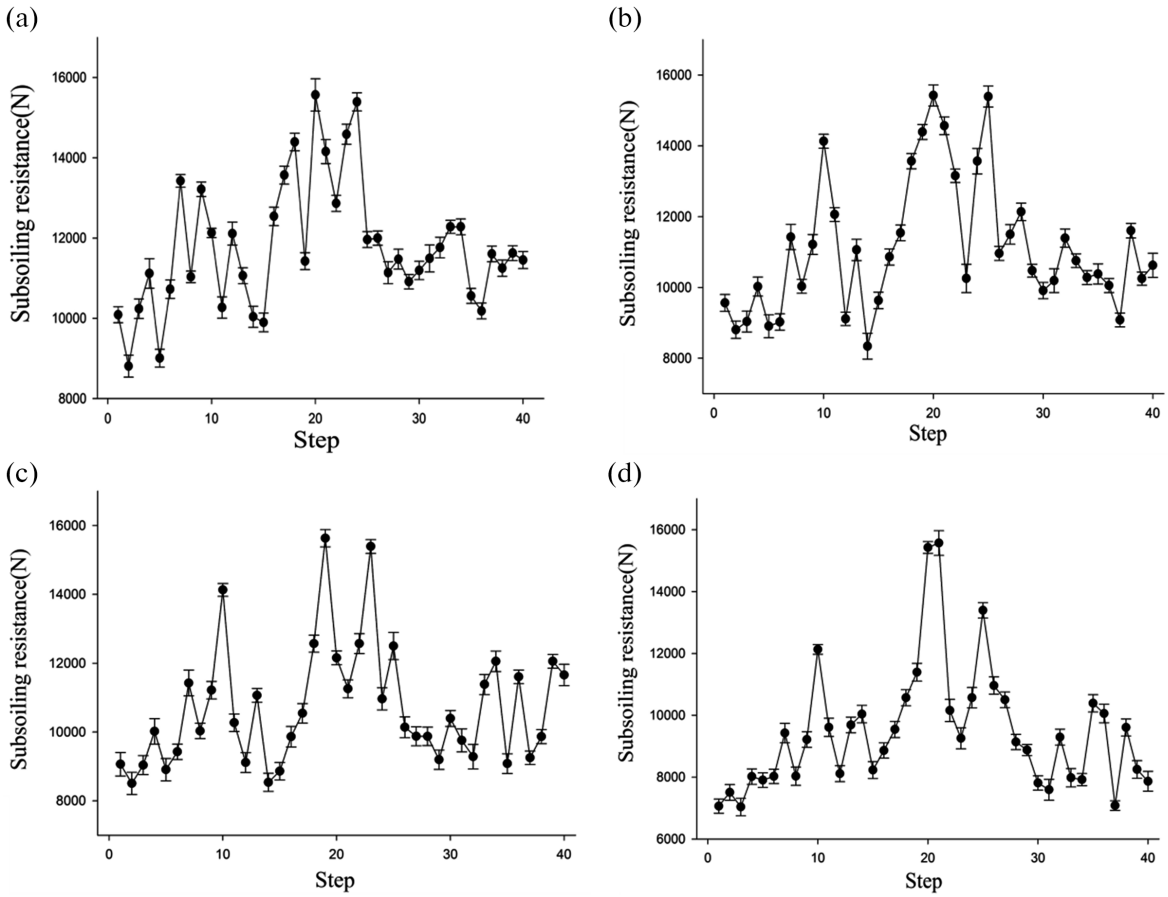

Fig. 17. Subsoiling drag reduction rate. The abscissa represents the working speed and the ordinate represents the pneumatic subsoiling drag reduction rate: (*a*) is the pneumatic subsoiling drag reduction rate when the working depth is 30 cm; (*b*) is the drag reduction rate of pneumatic subsoiling when the working depth is 35 cm; (*c*) is the drag reduction rate of pneumatic subsoiling when the working depth is 40 cm. [Colour online.]

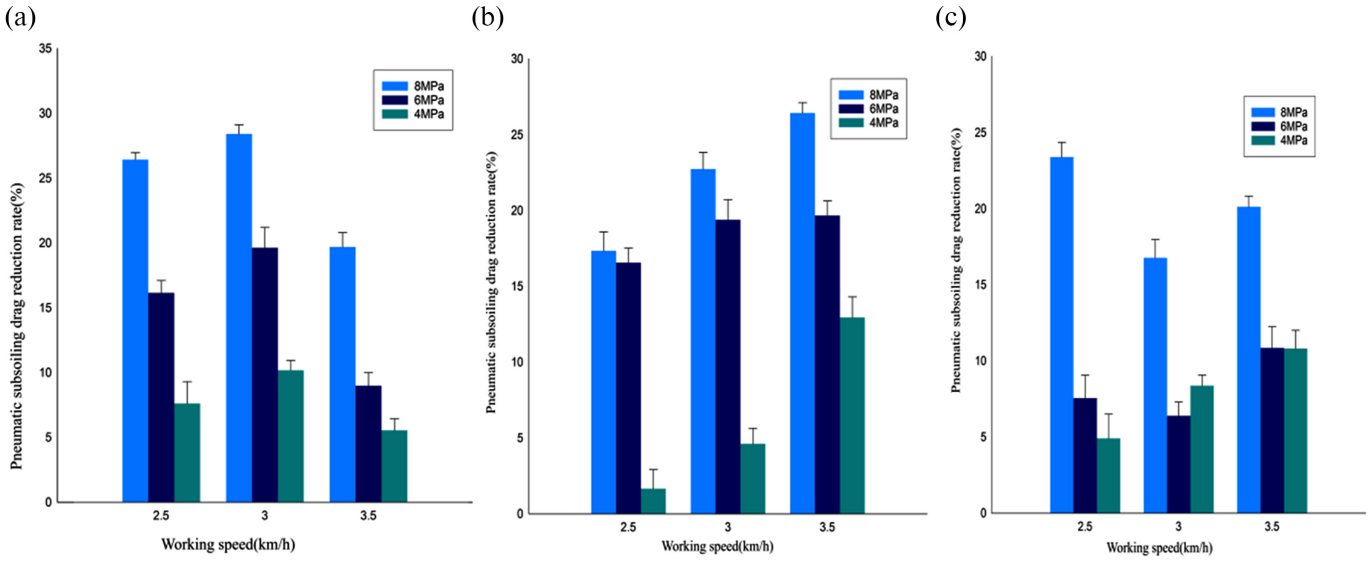

Table 4. Drag reduction rate of pneumatic subsoiling.

Working pressure P = 4 MPa									
Tillage depth (cm)	30			35			40		
Tillage speed (km·h^{-1})	2.5	3.0	3.5	2.5	3.0	3.5	2.5	3.0	3.5
Drag reduction percentage (%)	5.5	10.1	7.6	1.6	4.6	12.9	4.9	8.3	10.8
Working pressure P = 6 MPa									
Tillage depth (cm)	30			35			40		
Tillage speed (km·h^{-1})	2.5	3.0	3.5	2.5	3.0	3.5	2.5	3.0	3.5
Drag reduction percentage (%)	16.1	19.6	8.9	16.5	19.3	19.6	7.5	6.3	10.8
Working pressure P = 8 MPa									
Tillage depth (cm)	30			35			40		
Tillage speed (km·h^{-1})	2.5	3.0	3.5	2.5	3.0	3.5	2.5	3.0	3.5
Drag reduction percentage (%)	26.4	28.4	26.4	17.3	22.7	26.4	23.3	16.7	20.1

Fig. 18. Change of traction resistance in pneumatic subsoiling: (*a*) shows the change of average traction resistance in the process of pneumatic subsoiling and the traction resistance decreases with the decrease of pressure; (*b*) the decrease rate of average traction resistance increases with the increase of air pressure.

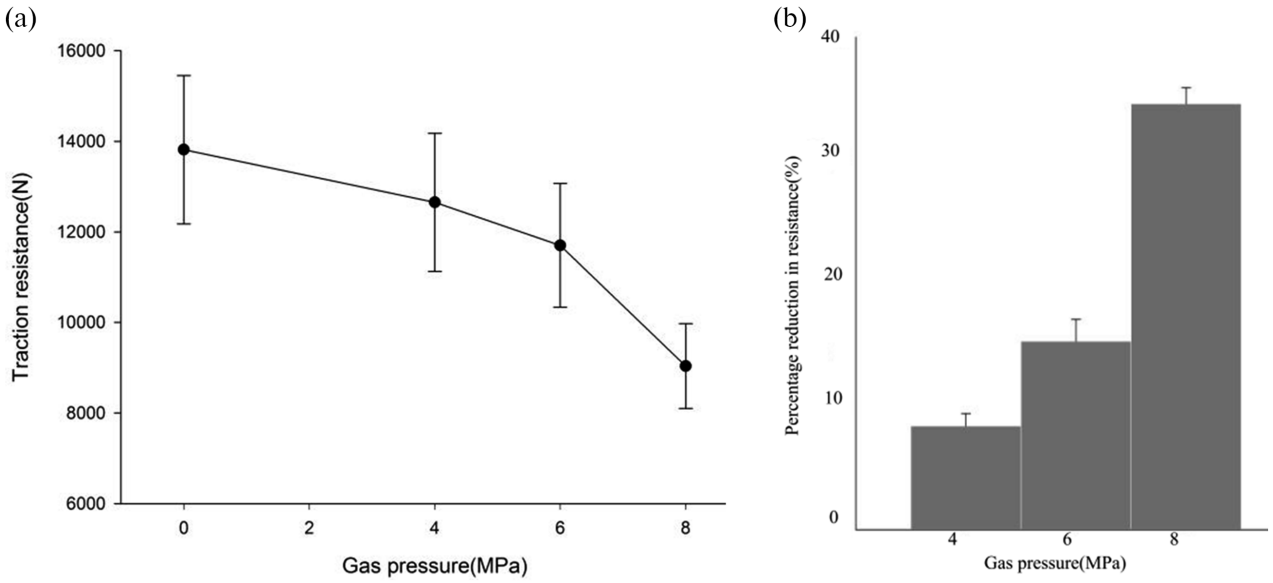

reduction effect became more and more obvious with the increase of air pressure. When the air pressure reached 8 MPa, the drag reduction effect was the most obvious because of high air pressure and strong instantaneous blasting force. The correlation coefficient between actual and predicted traction resistance was 0.9816. When the air pressure was 6 MPa, the drag reduction effect was obvious, and the correlation coefficient between actual and predicted traction resistance was 0.9837. When the air pressure was 4 MPa, the drag reduction effect was general, the maximum drag reduction rate was 8.42%, and the correlation coefficient between actual and predicted traction resistance was 0.9276. The results showed that there was a significant relationship between the actual traction resistance and the predicted traction resistance under the working pressure of this group ($P < 0.1$).

Evaluation results of pneumatic subsoiling operation

According to the working performance and quality regulations specified in the operation quality of subsoiling and trailing stubble machinery in China (ISO NY/T 1418-2021.0), pneumatic subsoiling was evaluated by ignoring the influence of depth and speed on disturbance according to eqs. 18 and 19. And the surface line of cultivated land, surface line of cultivated land and bottom

Table 5. Average values of the traction resistance.

	No air pressure (0 MPa)	Air pressure I (4 MPa)	Air pressure II (6 MPa)	Air pressure III (8 MPa)
Average value (N)	13 816	12 653	11 702	9036
Standard deviation (N)	1635	1524	1368	935
Drag drop percentage (%)		8.4	15.3	34.5
CV (%)	11.8	12.0	11.6	10.3

Note: CV, coefficient of variation. It is a statistic of the degree of variation of the measured values in the measured data. It is defined as the ratio of standard deviation to mean CV = $\frac{\sigma}{\mu}$. Data are desirable at CV < 15%.

Fig. 19. Comparison between simulated and actual traction resistance, in which the solid line represents the predicted traction resistance (SPR) and the dotted line represents the actual traction resistance (PR). Red represents 8 MPa, green represents 6 MPa and blue represents 4 MPa. (*a*) Under the condition of a working depth of 40 cm. (*b*) Under the condition of a working depth of 35 cm. (*c*) Under the condition of a working depth of 30 cm. [Colour online.]

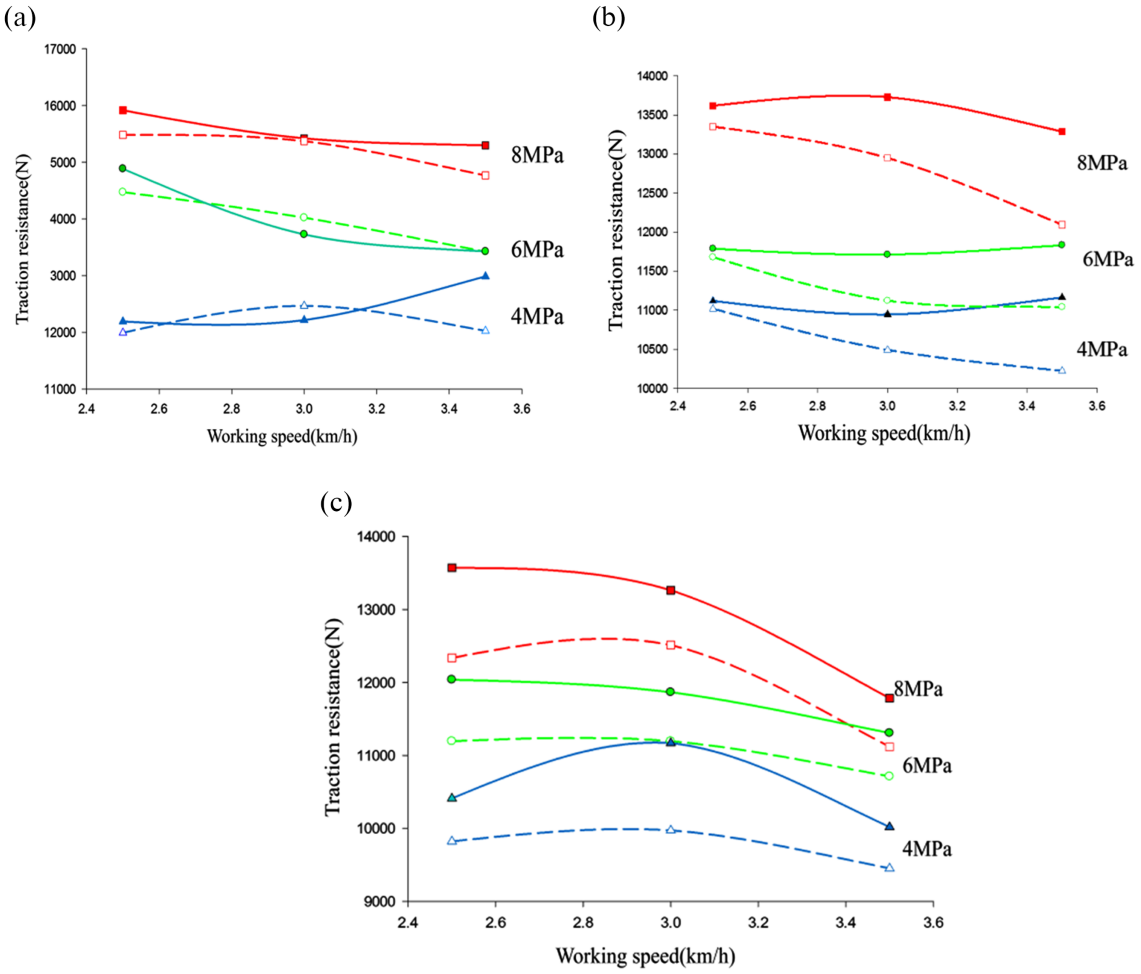

line of actual subsoiling ditch measured by subsoiling in the test were measured (as shown in Figs. 20*a* and 20*b*). The soil fluffy degree was 16.47%, lower than 40% of the evaluation standard; The soil disturbance coefficient was 55.49%, which was greater than 50% of the evaluation standard (as shown in Fig. 20*c*), indicating that the subsoiling effect have met the requirements. See Table 6 for soil fluffy degree and soil disturbance coefficient.

According to eq. 40, the cross-sectional area (tillage cross-sectional area) from the cultivated surface to the theoretical subsoiling ditch bottom is analyzed and compared, as shown in Fig. 20*d*. Ignoring the influence of working depth and working speed, when the working pressure was 4 MPa, the correlation coefficient between actual and predicted tillage cross-sectional area was 0.9588; The working pressure was 6 MPa, and the

Fig. 20. Measurement and prediction of soil fluffy degree and disturbance coefficient: (*a*) measurement of cultivated land surface line, cultivated land surface line and actual subsoiling ditch bottom line in the test; (*b*) soil cross-section model; (*c*) soil evaluation coefficient, and the error line represents the evaluation error; (*d*) the cross-sectional area of actual farming work is the same as that of predicted farming work. Black represents the cross-sectional area of actual farming work and gray represents the cross-sectional area of predicted farming work. [Colour online.]

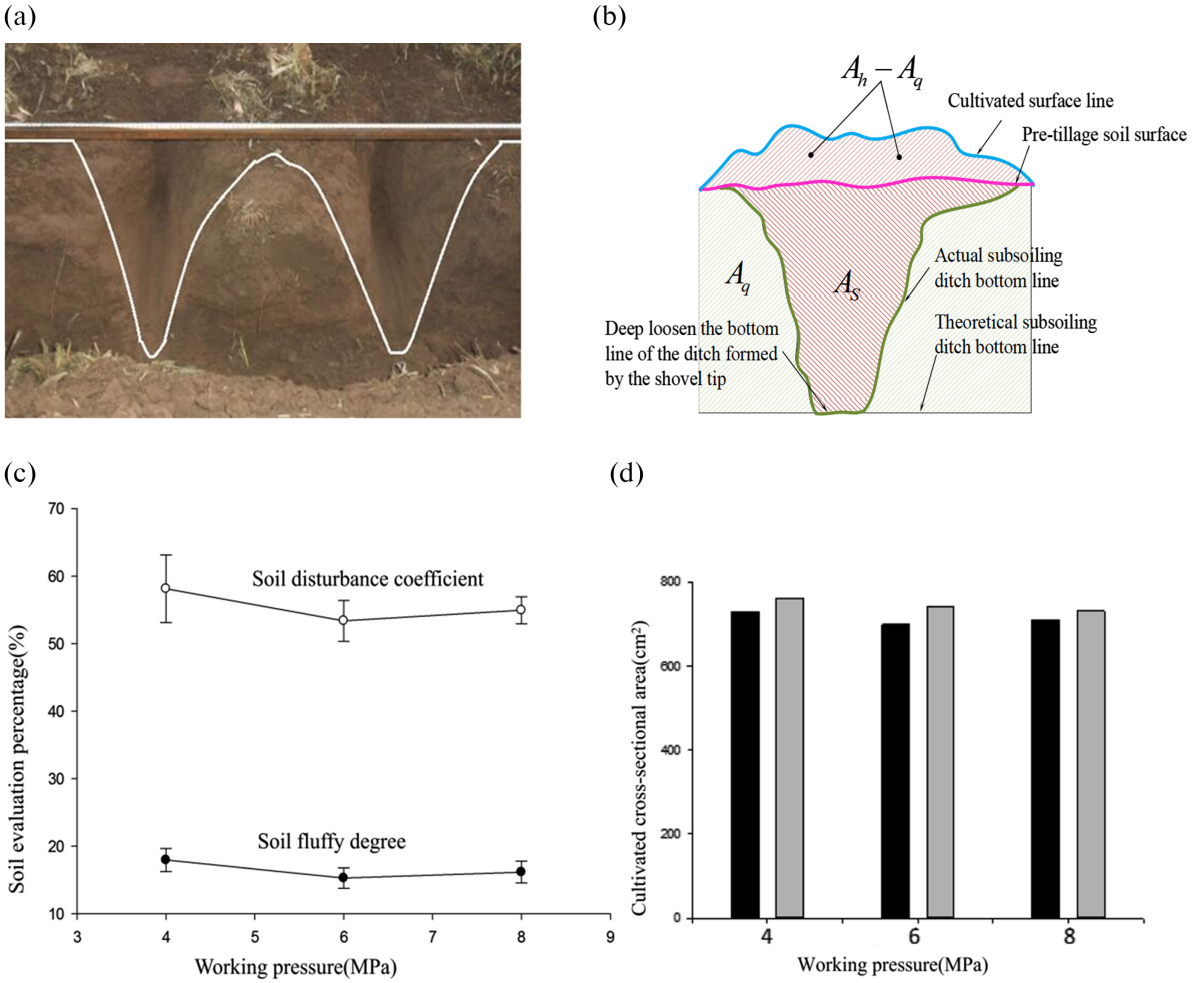

Table 6. Soil fluffy degree and soil disturbance coefficient.

Pressure (MPa)	A_h·cm^{-2}	A_q·cm^{-2}	A_s·cm^{-2}	Soil bulkiness (%)	Soil disturbance number (%)
4	729	618	359	17.9	58.1
6	698	605	323	15.2	53.3
8	709	610	335	16.1	54.9
Average	712	611	339	16.4	55.4

correlation coefficient between actual and predicted tillage cross-sectional area was 0.9427. The working pressure was 8 MPa, and the correlation coefficient between actual and predicted tillage cross-sectional area was 0.9715. The results showed that there was a significant relationship between actual tillage cross-sectional area and predicted tillage cross-sectional area under this group of working pressure ($P < 0.1$). However, in the process of pneumatic subsoiling, it can be clearly found that the correlation coefficient between working pressure and soil tillage cross-sectional area was 0.0608, and the relationship was not significant ($P > 0.1$), indicating that there was no relationship between air pressure and soil tillage cross-sectional area. It can be seen from Table 6 that in the process of pneumatic subsoiling, the high-pressure jet does not have too much impact on the cross-sectional area of soil tillage. When the air pressure was 4 MPa, the soil disturbance rate and soil fluffy

degree were greater than 6 and 8 MPa, so the high air pressure can reduce the tillage traction resistance, but it is impossible to increase the soil disturbance rate.

Conclusion

In this paper, a wheeled pneumatic blasting subsoiler was developed. Different from the traditional subsoiler, the subsoiler was operated by tractor. Subsoiling device is a "protective" soil improvement tool integrating "pneumatic subsoiling." Based on the analysis of traditional subsoiling machine by Jiang et al. (2020), this paper established a model for predicting traction resistance and a model for predicting tillage cross section. The main research goal of this paper was to predict the traction resistance of pneumatic subsoiling, and based on Wang et al. (2019), in this paper, nine different experimental groups were used to test the pneumatic subsoiling. The field test could verify the effectiveness of the traction resistance prediction model, and the performance analysis was compared with the conventional subsoiling machine. The prediction model in this paper could effectively predict the traction resistance and soil tillage cross-section area in the farming process, and the results were compared with the empirical expectation. The correlation between the measured traction resistance and the actual traction resistance was significant ($P < 0.1$). The correlation between the predicted tillage cross-section area and the actual tillage cross section was significant ($P < 0.1$). The model can be used to predict the traction resistance of pneumatic subsoiling machine and provide reference for the cultivation research of pneumatic subsoiling. The advantages of the model are suitable for practical application. As a part of this study, the influence of the change of model input on the variation percentage of model output was considered. The research showed that compared with the traditional subsoiling method, pneumatic subsoiling could reduce the traction resistance in the subsoiling process. Under three different air pressures, the traction resistance of the designed pneumatic subsoiling machine was reduced by 7.28%–22.37%, the soil disturbance coefficient was 55.49%, exceeding 50% of the evaluation standard, and could effectively achieve subsoiling. According to the pneumatic subsoiling mathematical model, a better air pressure can be designed to disturb the bottom of the plow, reduce the tillage resistance, and further optimize the energy and efficiency, so as to achieve the purpose of deep loosening and reducing resistance and energy consumption.

Acknowledgments

This study was supported by the general project of National Natural Science Foundation of China (No. 32171902, No.32060417) and the project of Tianjin Natural Science Foundation (No. 18jcybjc19300). We are grateful for the financial support.

References

Aday, S.H., and Ramadhan, M.N. 2019. Comparison between the draft force requirements and the disturbed area of a single tine, parallel double tines and partially swerved double tines subsoilers. Soil Till. Res. **191**. doi:10.1016/j.still.2019.02.011.

Ahmadi, I. 2017. Effect of soil, machine, and working state parameters on the required draft force of a subsoiler using a theoretical draft-calculating model. Soil Res. **55**: 389–400. doi:10.1071/sr16193.

Alakukku, L. 1999. Subsoil compaction due to wheel traffic. Agric. Food. Finland **8**(4): 333–351. doi:10.1016/s0167-8809(98)00167-4.

Alfaro, M.C., and Wong, R.C.K. 2001. Laboratory studies on fracturing of low-permeability soils. Can. Geotech. J. **38**(2): 303–315. doi:10.1139/cgj-38-2-303.

Askari, M., Shahgholi, G., and Abbaspour-Gilandeh, Y. 2019. New wings on the interaction between conventional subsoiler and paraplow tines with the soil: effects on the draft and the properties of soil. Arch. Agron. Soil Sci. **65**(1). doi:10.1080/03650340.2018.1486030.

Bandalan, E.P., Salokhe, V.M., and Gupta, C.P. 1999. Performance of an oscillating subsoiler in breaking a hardpan. J. Terramech. **36**(2): 117–125. doi:10.1016/s0022-4898(98)00035-4.

Cassman, K.G., Dobermann, A., and Walters, D.T. 2002. Agroecosystems, nitrogen-use efficiency, and nitrogen management. Ambio, **31**(2): 132–140. doi:10.1579/0044-7447-31.2.132.

Clark, R.L. 1999. Evaluation of the potential to develop soil strength maps using a cone penetrometer. ASAE Paper No. 99 3109, ASAE, 2950 St. Joseph, MI 49085–9659.

Coduto, D.P. 2001. Foundation design: principles and practices. Prentice-Hall: Chicago, IL.

Ess, D.R., Vaughan, D.H., and Perumpral, J.V. 1998. Crop residue and root effects on soil compaction. Trans. ASAE **41**(5). doi:10.13031/2013.17294.

Ferdinand, P., Russell, J., Phillip, J., and Brain, P. 2007. Kinetics of particles: energy and momentum methods, 10th ed. Indian Institute of Technology, Delhi (Chapter 13).

Figueiredo, E. B., and La Scala, N. 2011. Greenhouse gas balance due to the conversion of sugarcane areas from burned to green harvest in Brazil. Agric. Ecosyst. Environ. **141**(1–2): 77–85. doi:10.1016/j.agee.2011.02.014.

Gordon, W.B., Whitney, D.A., and Fjell, D.L. 1998. Starter fertilizer effects on grain sorghum hybrids grown on a soil high in residual phosphorus in a no-tillage environment. J. Plant Nutr. **21**(11): 2403–2415. doi:10.1080/01904169809365573.

Hang, C., Gao, X., Yuan, M., et al. 2017. Discrete element simulations and experiments of soil disturbance as affected by the tine spacing of subsoiler. Biosyst. Eng., 73–82. doi:10.1016/j.biosystemseng.2017.03.008.

Hilal, Y.Y., Al-Rajabo, S., and Dahham, G.A. 2021. The effects of vibrating wings subsoiler plow on driver's seat of agricultural tractors and mechanization performance. Soil Till. Res. **205**. doi:10.1016/j.still.2020.104806.

Hipps, N.A., and Hodgson, D.R. 1987. The effect of a slant-legged subsoiler on soil compaction and the growth of direct-drilled winter wheat. J. Agric. Sci. doi:10.1017/S0021859600081028.

ISO NY/T 1418-2021.0. Technical specification for quality evaluation of subsoiling machinery.

Jawoski, W., Duncan, J.M., and Seed, H.B. 1981. Laboratory study of hydraulic fracturing. J. Geotech. Eng. Div., ASCE **107**(6): 713–732. doi:10.2514/3.56113.

Jia, H., Guo, M., Yu, H., and Li, Y. 2016. An adaptable tillage depth monitoring system for tillage machine. Biosyst. Eng. doi:10.1016/j.biosystemseng.2016.08.022.

Jiang, X., Tong, J., Ma, Y., and Sun, J. 2020. Development and verification of a mathematical model for the specific resistance of a curved subsoiler. Biosyst. Eng. **190**(C). doi:10.1016/j.biosystemseng.2019.12.004.

Khalilian, A., Han, Y.J., Marshall, M.W., Gorucu, S., Abbaspour-Gilandeh, Y., and Kirk, K.R. 2014. Evaluation of the Clemson instrumented subsoiler shank in coastal plain soils. Comput. Electron. Agric. **109**: 46–51. doi:10.1016/j.compag.2014.09.002.

Lin, Y., Yang, L., Liu, S., Zhao, X., Cao, C., and Li, C. 2019. Virtual simulation technology based research on subsoiling process. Int. J. Eng. Res. **233**(5): 1493–1503. doi:10.1177/0954406218774358.

Murdoch, L.C. 2002. Mechanical analysis of idealized shallow hydraulic fracture. J. Geotech. Geoenviron. Eng. **128**(6): 488–495. doi:10.1061/(asce)1090-0241(2002)128:6(479).

Nautiyal, D. 1994. Fluid flow modeling for pneumatically fractured formations. New Jersey Institute of Technology, New Jersey.

Puppala, S. 1998. Pneumatic fracture propagation and particulate transport in geologic formations. New Jersey Institute of Technology, New Jersey.

Raper, R.L., Schwab, E.B., and Dabney, S.M. 2005. Measurement and variation of site-specific hardpans for silty upland soils in the Southeastern United States. Soil Tillage Res. **84**(1): 7–17. doi:10.1016/j.still.2004.08.010.

Sanchez, C., Arribart, H., and Guille, M.M.G. 2005. Biomimetism and bioinspiration as tools for the design of innovative materials and systems. Nat. Mater. **4**: 277–288. doi:10.1038/nmat1339. PMID:15875305.

Simoes, D., Silva, M.R.D., and Fenner, P.T. 2011. Operational performance and costs of the subsoiling operation in eucalypt implantation area. Biosci. J. **27**(5): 692–700.

Usaborisut, P., and Prasertkan, K. 2019. Specific energy requirements and soil pulverization of a combined tillage implement. Heliyon **5**(11). doi:10.1016/j.heliyon.2019.e02757.

Wang, Z.F., Shen, S.L., and Modoni, G. 2019. Enhancing discharge of spoil to mitigate disturbance induced by horizontal jet grouting in clayey soil: Theoretical model and application. Comput. Geotech. **111**(JUL.): 222–228. doi:10.1016/j.compgeo.2019.03.012.

Ywa, B., Na, L.A., Ym, A., Tong, J., Pfleging, W., and Suna, J. 2020. Field experiments evaluating a biomimetic shark-inspired (BioS) subsoiler for tillage resistance reduction. Soil Till. Res. **196**. doi:10.1016/j.still.2019.104432.

Zhang, H., Araya, K., Kudoh, M., Zhang, C., Jia, H., Liu, F., et al. 1999. An explosive subsoiler for the improvement of meadow soil, part 3: field experiments. J. Agric. Eng. Res. **75**(3): 327–332. doi:10.1006/jaer.1999.0517.